Gao, Z, Chen, Y, Kulczyk-Malecka, J, Kelly, P, Zeng, Y, Zhang, X, Li, C, Liu, H, Rohbeck, N and Xiao, P (2018) Comparison of the oxidation behavior of a zirconium nitride coating in water vapor and air at high temperature. Corrosion Science, 138. pp. 242-251. ISSN 0010-938X

DOI: https://doi.org/10.1016/j.corsci.2018.04.015

Publisher: Elsevier

Version: Accepted Version

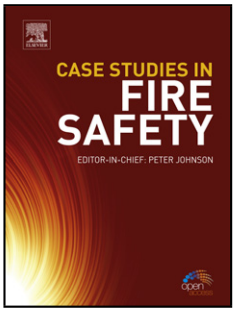

Title: Comparison of the oxidation behavior of a zirconium nitride coating in water vapor and air at high temperature

Authors: Zhaohe Gao, Ying Chen, Justyna Kulczyk-Malecka, Peter Kelly, Yi Zeng, Xinxin Zhang, Chun Li, Han Liu, Nadia Rohbeck, Ping Xiao

PII: S0010-938X(17)30923-X
DOI: https://doi.org/10.1016/j.corsci.2018.04.015
Reference: CS 7481

To appear in:

Received date: 21-5-2017
Revised date: 3-4-2018
Accepted date: 9-4-2018

Please cite this article as: Gao Z, Chen Y, Kulczyk-Malecka J, Kelly P, Zeng Y, Zhang X, Li C, Liu H, Rohbeck N, Xiao P, Comparison of the oxidation behavior of a zirconium nitride coating in water vapor and air at high temperature, *Corrosion Science* (2010), https://doi.org/10.1016/j.corsci.2018.04.015

Comparison of the oxidation behavior of a zirconium nitride coating in water vapor and air at high temperature

Zhaohe Gao[a], Ying Chen[a], Justyna Kulczyk-Malecka[a,b], Peter Kelly[b], Yi Zeng[a], Xinxin Zhang[a], Chun Li[a], Han Liu[a], Nadia Rohbeck[a] and Ping Xiao[a*]

[a]*School of Materials, University of Manchester, Manchester UK, M13 9PL, UK*

Highlights

- The parabolic rate constant of ZrN oxidizing in water vapor environment at 600 °C was approximately 100 times faster than that in air, due to larger pores and more cracks were formed across ZrO_2 layer formed during the water vapor oxidation process than during the air.
- The bilayer-structure of ZrO_2 with t-ZrO_2 near ZrN-ZrO_2 interface and m-ZrO_2 closing to the outer oxide surface were formed after water vapor or air oxidation.
- The lateral cracks across the ZrO_2 scale were caused by the phase transition from t-ZrO_2 to m-ZrO_2.

[b]School of Research, Enterprise and Innovation, Manchester Metropolitan University, Manchester, M1 5GD, UK

Abstract:

The oxidation behavior of zirconium nitride coating in high-temperature water vapor and air environments was studied. The parabolic rate constant of ZrN oxidizing in the water vapor environment at 600 °C was approximately 100 times faster than that in air, due to the larger pores and greater number of cracks that were formed across ZrO_2 oxide layer formed during the water vapor oxidation process than during the air oxidation process. A bilayer-structure ZrO_2 with tetragonal ZrO_2 near the ZrN/ZrO_2 interface and monoclinic ZrO_2 approaching the outer ZrO_2 surface were formed in both cases. The lateral cracks across the ZrO_2 scale were caused by volume expansion from the tetragonal ZrO_2 phase to the monoclinic ZrO_2 phase transition.

Corresponding author: Ping Xiao (p.xiao@manchester.ac.uk)

Keywords: zirconium nitride; water vapor; oxide cracks; phase transition; oxidation kinetic; oxidation mechanism

1. Introduction

Since the nuclear disaster occurred at the Fukushima Daiichi Power Plant on March 2011 owing to a Loss-of-Coolant Accident (LOCA) in the Light Water Reactor, concerns over the safety of nuclear power plants in the case of a cooling system failure have been raised. When a LOCA occurs, the zirconium fuel cladding quickly reacts with the high-temperature water vapor generated by the fission product decay heat trapped inside the nuclear reactors [1, 2]. The reaction produces a large amount of hydrogen in a short period of time, which is highly flammable and upon ignition can lead to an explosion.

One potential strategy to mitigate LOCA from occurring is to apply an oxidation-resistant coating onto the surface of the zirconium fuel cladding. To date, a few metallic (e.g. FeCrAlY) and ceramic (e.g. Ti_2SiC, TiN) coatings have been deposited on zirconium alloys and been tested in different environments [3, 4]. These coatings have been shown to slow down the oxidation rate of the zirconium alloys in air or water vapor to a certain extent. However, none of these coatings have shown satisfactory durability which is required in case of failure of the cooling system in nuclear power plants.

From the perspective of practical application, an effective coating on the zirconium fuel cladding should be protective, thermally stable, thermally conductive, well-adhered to the metal substrate, mechanically robust and have a low neutron capture cross-section. A potential candidate material that meets these criteria, apart from the coating materials reported in the literature, is zirconium nitride (ZrN). The main reasons that ZrN coating is good candidate are its high oxidation resistance, high thermal conductivity and low neutron capture cross-section [5-7]. The majority of current studies of ZrN have focused on its oxidation behavior and products in air, which is significantly different from the high temperature water vapor environment encountered by the zirconium fuel cladding in case of cooling system failure[8, 9].

Harrison, Lee, and Jacobson studied the oxidation of ZrN from 973-1373K under static air conditions and reported a parabolic rate behavior indicative of a diffusion-controlled process[8]. Others have confirmed that the oxidation kinetics of ZrN in the high temperature air follows a parabolic relation while there are disagreements related to the phase structure (tetragonal or monoclinic) of the ZrO_2 formed on the ZrN[10]. To the best of our knowledge, we are not aware of any study of the oxidation behavior and oxidation kinetics of ZrN in a water vapor environment at high temperature. It is expected that metals and ceramics show different oxidation behavior and oxidation mechanism in air and steam at high temperature. For example, Kyung Tae Kim, et al, found that the high-temperature (700°C to 1200°C) oxidation kinetics of Zr alloy in the air were more rapid than that in the steam[11]. Dong Jun Park, et al, reported that the SiC showed two different oxidation behaviors in the air and water vapor environment at 1200°C and SiC underwent weight gain and weight loss during oxidation in air and steam, respectively[12].

To address this research gap and to understand the oxidation behavior of ZrN in water vapor and test if ZrN might be used as an effective coating material in zirconium fuel cladding, the oxidation behavior of a ZrN coating deposited on a zirconium alloy substrate in high temperature water vapor was systematically studied in this work. The ZrN coating was deposited using reactive magnetron sputtering, a technique, which offers excellent uniformity of the coating layer. The oxidation behavior of the ZrN coating in air was also studied in order to compare the difference of the oxidation behavior and oxidation kinetics of the coating in these two environments.

Finally, observation of the ZrO_2 scales formed on the ZrN after oxidation in an air environment has revealed the existence of cracks and pores [9]. The phase structure of the ZrO_2 and the cracks themselves are generally believed to play an import role in the oxidation process of ZrN during high-temperature air[8]. However, it is not fully understood how the cracks are generated and the effects of oxide scale on the oxidation mechanism of ZrN in the air. And the morphology of the oxide scale formed on ZrN in the water vapor environment at high temperature and the related oxidation mechanism are also unknown. Thus, the formation mechanism of cracks and pores and the effect of the oxide scales on the oxidation mechanism of ZrN in the high temperature air and water vapor have also been studied.

2. Experiments

2.1 Sample preparation and oxidation test

The ZrN coatings were deposited on Zr2.5wt%Nb alloy coupons (100 ×50 × 2 mm^3), which were ultrasonically pre-cleaned in acetone. Deposition took place by reactive sputtering in a Teer Coatings UDP 350 closed field unbalanced magnetron sputtering system, described in detail elsewhere [13]. Two vertically mounted magnetrons (300 x 100 mm^2) were installed in opposed positions through the chamber walls in a closed field configuration, with a centrally mounted rotating substrate holder. A 99.5% pure Zr target was fitted to one of the magnetrons and the second magnetron was blanked off; it was present only to close the magnetic field lines across the chamber. Prior to deposition, the chamber was pumped down to a base pressure of lower than $1x10^{-3}$ Pa and then backfilled to a working pressure of 0.3 Pa with argon. The substrates were sputter cleaned at a bias voltage of -800V DC for 10 mins. The zirconium target was powered by a dual channel Advanced Energy Pinnacle Plus power

supply operating in pulsed DC mode at an average power of 1 KW and a pulse frequency of 100kHz with a 4.0 µs off time (duty cycle = 60%). To ensure good coating to substrate adhesion, an initial 50nm interlayer of pure zirconium was deposited in an argon only atmosphere. The optical emission monitoring (OEM) system was used to control the amount of nitrogen introduced into the system during the deposition of ZrN films, using settings based on previous experience to produce a stoichiometric coating[13, 14]. The Ar flow rate was 20 standard cubic centimetres per minute (SCCM) and N_2 was controlled using optical emission monitor (OEM) set at 50% total metal (Zr) signal. A bias of -50 V was applied to the substrate throughout coating deposition. The substrate temperature under the sputtering conditions was below 200°C. Rectangular samples (10×10mm) were cut from the ZrN-coated alloy plates using a SiC abrasive cutting blade in a precision cut-off machine (Accutom 5, Struers). The samples were then cleaned with soap water and acetone.

Oxidation in water vapor was conducted by flowing a mixture of argon and water vapor through a universal tube furnace (Carbolite, UK) at 600 °C for different periods of time up to 2 hours. The flowing argon first flowed through a flask containing ~ 400 ml boiling water which generated sufficient amount of water vapor. The water vapor was then carried by the flowing argon to the hot zone of the furnace where the samples were placed.

In order to control the volume content of the water vapor during oxidation, the mass of the flask before and after the experiment was measured. The volume of the water vapor flowing over the surface of the sample was 1.74 L/min. Oxidation in air was conducted by placing the samples in the centre of the hot zone of the same furnace and heating it up to 600°C in the ambient flowing air. In order to minimise the oxidation during ramping and down, the samples were directly put inside the furnace when the temperature stabilised at 600°C and then taken out after oxidation.

2.2Microstructural characterization and stress measurement

The phase composition of the ZrN coating and oxides was analysed by grazing incidence X-ray diffraction (GIXRD, Philips X′pert) using Cu Kα radiation (λ=1.5406 Å). The surface and cross-section of the ZrN coatings and oxides were investigated by scanning electron microscopy (SEM, FEI, Quanta 650) coupled with a focused ion beam (FIB, FEI, Quanta 3D). The thickness of the oxides was estimated from the cross-section exposed by FIB milling through the surface. Tilt correction was implemented to compensate for the distortion of the image induced by tilting. To observe the microstructure of the oxides in greater detail, thin lamellas of the cross-sections of the oxides were prepared by FIB using the *in situ* lift-out technique and then examined using transmission electron microscopy (TEM, FEI, Tecnai G2).The phase distribution in the oxides was mapped using a transmission electron backscatter diffraction performed on an FEI Magellan 400 XHR scanning electron microscope (SEM). This technique is known for its high resolution, which has been shown to be particularly useful in analysing materials with fine grains. More details of this technique can be found elsewhere [15]. The Gibbs reaction energy between ZrN and oxygen and ZrN and water vapor, was calculated using Thermocalc 4.0 software and the calculation followed the Calphad rules.

The biaxial stress in the ZrO_2 oxide layer was measured by XRD using the $\sin^2\psi$ method carried out in a Bruker D8 Discover x-ray diffractometer. An X-ray tube (Co, λ=1.789 Å) was fixed with an incident beam angel of 5° during the measurement. The detector enables the ψ (the angle between the surface normal and the bisector of the incident and diffracted beam) offset to be measured simultaneously. Co Kα radiation (λ_{Co} = 1.78897Å) was used to acquire the diffraction peak from the (-1 1 1) plane of monoclinic ZrO_2 for all the measurements. The geometry configuration is shown in Fig.1. The XRD measurements give a series of d-spacing values corresponding to different ψ angles. These d-spacing values were then plotted against $\sin^2 \psi$, which were then fitted with a straight line. The slope of the line was used to calculate the residual stress (σ) according to the formula [16, 17]:

$$\sigma = (\frac{E}{1+v})_{e\ \mathrm{hkl}\mathcal{E}}\ \frac{1}{d_n}\frac{(d_\omega - d_n)}{sin^2\omega}$$

where E and ν are the elastic modulus (243 GPa) and Possion’s ratio (0.28) of the (-1 1 1) plane, respectively[18]. And value of d_n was the d-spacing along the surface normal (when ψ=0). The d_n was estimated based on the (-1 1 1) diffraction peak using Cu Kα radiation (λcu = 1.5406Å) under the ϴ/2ϴscanning configuration in a powder X-ray diffractometer (Philips PANalytical X′Pert).

3. Results

3.1 As-deposited ZrN coating

Fig.2 a shows a cross-sectional SEM micrograph of the ZrN coating, which is about 1.8µm thick, smooth, fully dense, gold colour, well-adhered to the substrate and there is no significant roughness, porosity or cracks. For the phase structure analysis of the as-deposited ZrN, the ex situ GIXRD was carried out. The ex situ GIXRD patterns show that the ZrN coating consists of cubic ZrN phase (ICDD 01-080-3718, a= 0.463nm) in Fig. 2b and no preferred orientation. The Zr peaks in the traces are from the substrate material. It can be observed that the ZrN (111) and (200) peaks become broader, indicating a fine grain sized structure.

3.2 Oxidation kinetics in water vapor and air environments

Fig.3 shows the change in oxide thickness as a function of time for ZrN oxidised in air and water vapor environments at 600°C. The oxidation rate was not directly measured in the high-temperature water vapor and air experiments. One way to determine the oxidation kinetics of the ZrN is to measure the thickness of the ZrO_2 layer formed on the surface of the ZrN coating after high-temperature water vapor and air oxidation. The rate change of the ZrO_2 layer formation after oxidation in the air reveals a classical parabolic curve (R^2, 0.995; k, 1.53×10^{-13} m^2s^{-1}) due to the increased diffusion distance for oxygen migrating through the growing ZrO_2 layer to the ZrO_2/ZrN reaction interface. The rate change of ZrO_2 layer formed on the ZrN in the 600°C water vapor environment shows satisfactory parabolic fit (R^2,0.982; k, $1.57 \times 10^{-11} m^2s^{-1}$). Comparing the data indicates that the parabolic rate constant of ZrN oxidizing in the 600°C water vapor is approximately 100 times higher than that in the 600°C air environment.

3.3 Oxidation behavior of ZrN in the high-temperature water vapor furnace

Fig.4a and b show the cross-sectional images of the ZrN coatings after oxidation in water vapor furnace at 600°C for 0.5 and 1 hour, respectively. After 0.5 hour oxidation, the ZrN is heavily oxidized, and the oxide layer shows evidence of porosity, as shown in the Fig.4 a. A greater number of cracks and pores are visible after oxidation at 600°C in water vapor for 1 hour (Fig. 4b). It also can be seen in fig. 4b that approximately half of the ZrN coating has been consumed up after oxidation at 600°C water vapor for 1 hour and the thickness of oxide layer is about 2.6 µm. The oxide layer contains many pores and cracks. However, it had not spalled from the ZrN coating. In order to study the potential for accident tolerance of ZrN coatings in the nuclear reactors, an additional 1200°C water vapor test was carried out. After oxidation in water vapor at 1200°C for 1 minute, the ZrN was almost completely consumed up and the oxide layer consisted of nano-scale pores and cracks, as shown in Fig.4c. It is hypothesized that these pores and cracks may be caused by bubbles containing gaseous reaction by-products.

Fig.5 is the GIXRD patterns of the ZrN coatings after oxidation at 600°C in water vapor for 1 hour. The oxide scale formed by consumption of ZrN is ascribed to the tetragonal (t)- ZrO_2 (JCPDS 50-1089) and monoclinic (m)- ZrO_2 (JCPDS 37-1484) phases. As the incidence angle increases from 2° to 3°, the peak intensity of monoclinic(m)-ZrO_2 decreases, whereas that of the tetragonal(t)-ZrO_2 and ZrN peaks increase. This indicates that the outer oxide layer is mainly composed of m-ZrO_2 and the interface oxide layer is mainly t-ZrO_2. This is in agreement with the oxidation products during oxidation of ZrN coating at 650°C in air presented elsewhere [9].

Fig.6 shows a cross-sectional bright field TEM image of the ZrO_2 oxide grown on the top of the ZrN coating after oxidation at 600°C in the water vapor for 1 hour. The interface between the nitride and oxide regions is flat. Based on the selected area diffraction patterns, the area A and B are mainly identified as tetragonal ZrO_2 and monoclinic ZrO_2, respectively. Based on the GIXRD and TEM results, it suggests that a bilayer structure with an inner layer of t- ZrO_2 and an outer layer of m- ZrO_2 closer to the oxide surface has been formed. Furthermore, many lateral micro-cracks and small pores, indicated as red arrows in the Fig.6, are observed throughout the ZrO_2 layer. The cracks are distributed uniformly not only in the interfacial t-ZrO_2 layer but also the m-ZrO_2 outer layer. These cracks are non-interconnected across the porous ZrO_2 layer and there are no visible vertical micro-cracks at the coating/substrate interface.

Fig.7 shows the t-EBSD cross-sectional phase map of the ZrO_2 layer. The m-ZrO_2 phase, as shown by the blue colour, is dominant in the outer oxide layer with minor traces of t-ZrO_2 which is mainly distributed in the ZrN/ZrO_2 interface region. The oxidation of ZrN is dominated by inward diffusion of oxygen or oxidizing species [8] and therefore this can be predicted that any new oxidation product of ZrN is solely composed of t-ZrO_2. The appearance of m-ZrO_2 could be related to the phase transition product from t-ZrO_2 as the m-ZrO_2 is known to be more stable than t-ZrO_2 below 1170°C. Based on the peak intensity of ZrO_2 from the by XRD and t-EBSD results, the phase content ratio m-ZrO_2/t-ZrO_2 is 1.5, which indicates that most of the t-ZrO_2 phases undergoes the phase transition to m-ZrO_2.

3.4 Oxidation behavior of ZrN in the high-temperature air furnace

Fig.8 shows cross-sectional SEM images of the ZrN coating after being oxidized in air. After oxidation at 600°C for 1 hour, the oxide layer formed on the top of ZrN is smooth and appears denser than that formed after water vapor oxidation, as shown in the Fig.8 a. Compared to the porous oxide layer after water vapor oxidation, there is a smaller amount of nano-scale lateral crack across the oxide layer, as it was apparent in ZrO_2 created during air oxidation (Fig.8 a). The thickness of the oxide layer is about 240 nm, which is about one tenth of the thickness of the ZrO_2 layer than that had grown after 1 hour exposure to water vapor oxidation at 600°C. This dense oxide layer serves as an oxidation resistant layer to protect the underlying ZrN coating from further oxidation.

The oxide layer became thicker as the oxidation time increased from 1 hour to 4 hours and eventually 8 hours, as shown in the Fig.8 b and c, respectively. Both images show that there are visible micro-scale cracks across the oxide layer and the cracks are non-uniformly distributed. The cracks are mainly lateral and no obvious vertical cracks can be observed. A large majority of non-interconnected cracks rumple across the oxide layer. However, the interface between the ZrN and ZrO_2 oxide layers and the surface of the oxide layer are flat. No spallation of oxide is observed, and therefore it can continue to fulfil the role of oxidation barrier layer for the underlying ZrN coating.

Fig.9 shows the ex situ GIXRD patterns of the ZrN coating after the coating was oxidised in air at 600°C for 8 hours. At 1° angel of incidence, the m-ZrO_2 peaks are dominant with minor traces of t-ZrO_2 and ZrN. As the incidence angle increase from 1° to 3°, the peak intensity of tetragonal (t)-ZrO_2 and ZrN peaks increase while that of monoclinic (m)-ZrO_2 decreases. Again, this indicates that the outer oxide layer is mainly composed of m-ZrO_2 and the interface oxide layer is mainly t-ZrO_2. The bilayer structure of ZrO_2 after oxidation in air at 600°C is similar to that found after water vapor oxidation.

Fig.10 is the cross-sectional bright field TEM image of the oxidized ZrN coating after 1 hour at 600°C in air. As mentioned, the thickness of ZrO_2 layer is about 240 nm, as shown in the Fig.10 a. The interface between the ZrN coating and the oxide can be clearly observed based on the EDS line scanning, as shown in Fig.10 b. There is only one visible nano-scale lateral crack and some nano-scale porosity. The ZrO_2 oxide in the interface between the ZrN and the oxide shows mainly a columnar structure, whereas the $Zr0_2$ in the outer layer is primarily equiaxed.

Fig.11 is the t-EBSD cross-sectional phase map of the ZrO_2 layer formed on the top of ZrN coating after 1 hour at 600°C in air. It can be clearly seen that the ZrO_2/ZrN interfacial oxide layer is predominately t-ZrO_2, as shown by green colour in Fig.11. Again, this indicates that any new oxide scale formed by consuming ZrN is initially solely composed of t-ZrO_2. The outer layer of the oxide scale is dominated by m-ZrO_2 with minor traces of t-ZrO_2. The phase content ratio m-ZrO_2/t-ZrO_2 is 1.2, which is lower than that after water vapor oxidation (1.5). Furthermore, the m-ZrO_2 is the product of the phase transition from t-ZrO_2 rather than direct oxidation of ZrN coating.

4. Discussion

4.1 Oxidation products of ZrN

Several studies have been focused on the investigation of the high-temperature air oxidation behavior of ZrN coatings [8,9]. However, there are disagreements on the phase structure of the ZrO_2 oxide scale that forms and there have been no previous investigation on the oxidation products of ZrN after high-temperature water vapor testing. In a high-temperature air environment, the ZrO_2 scale forms on the surface of the ZrN coating by inward diffusion of oxygen, which has been demonstrated elsewhere by a gold marker experiment[19]. Similarly, the oxidation product of ZrN after high-temperature water vapor oxidation is ZrO_2, as confirmed by GIXRD and TEM analyses. The reaction between ZrN and oxygen/water vapor can be written as follows:

$$2ZrN + 2O_2 = 2ZrO_2 + N_2 \qquad \Delta G(873.15K,)= -1290.4KJ \quad (1)$$

$$2ZrN + 4H_2O = 2ZrO_2 + N_2 + 4H_2 \qquad \Delta G(873.15K,)=-514.7KJ \quad (2)$$

Where, the ZrO_2 is tetragonal, temperature is 873.15K. Based on the equations 1 and 2, the Gibbs energy of the two reactions is negative and the water vapor oxidation process of ZrN also generates the hydrogen gas besides nitrogen. The required activation energy to convert ZrN to t-ZrO_2 is less than that needed to transformed ZrN to m-ZrO_2 although the m-ZrO_2 is more stable than t-ZrO_2 below 1170°C[9]. However, in this work, t-ZrO_2 was the only phase of the oxide detected by t-EBSD and TEM at the ZrN/ZrO_2 interfacial region, indicating that the new oxide formed by oxidizing ZrN is solely composed of t-ZrO_2. The existence of m-ZrO_2 can be explained that the m-ZrO_2 generation from the martensitic phase transition from t-ZrO_2. The existence and transition of two different ZrO_2 phase are in agreement with the oxidation behavior of ZrN at 650°C in an air environment[9].

The mechanism for the phase stabilization of metastable t-ZrO_2 could be proposed from the viewpoints of a stress induced effect, grain size refinement and formation of oxygen ion vacancies [20]. As deduced from recent studies on the oxidation of ZrN [8], the stress state is the key factor influencing the phase transition of the ZrO_2 scale. Using the $Sin^2ψ$ method in this study, the stress (including the growth stress and thermal stress) in the m-ZrO_2 oxide scale after water vapor and air test was measured as 200 MPa and 1.2 GPa (compressive stress), respectively. The thermal stress σ in m-ZrO_2 has been calculated to be 160 MPa (tensile stress), based on the following equation[21].

$$\sigma=E\Delta T\Delta\alpha/(1-\nu)$$

Where $\Delta T\approx580°C$, and the thermal expansion coefficients α ($10^{-6}K^{-1}$) are 6.5 for m-ZrO_2 and 5.7 for Zr alloy, respectively.

It is well known that the stress in the oxide scale depends on the competition between stress generation and relaxation [22]. In this study, the growth stress can generate the compressive stress during oxidation process as there is constrained molar volume expansion from ZrN to t-ZrO_2, and finally to m-ZrO_2[9, 15]. Furthermore, there is a stress gradient and the compressive stress decreases from ZrN/t-ZrO_2 interface to the outer oxide surface[9, 15]. As the compressive stress decreases from the interface to the surface of the ZrO_2 layer, there is a critical point of compressive stress where the t-ZrO_2 cannot be stabilised by compressive stress and therefore the transition from t-ZrO_2 to m-ZrO_2 occurs. This results in the formation of a bilayer-structure of ZrO_2 with t-ZrO_2 near the ZrN/ZrO_2 interface and m-ZrO_2 closer to the outer oxide surface. The phase content of m-ZrO_2 after water vapor oxidation is higher than that after air oxidation, which can be explained by the relaxation of compressive stress. The compressive stress in the oxide scale after water vapor test is 200 MPa, whereas the stress present in the oxide scale after air test is 1.2GPa. The compressive stress values of m-ZrO_2 vary from ~100MPa to ~2GPa depending on the oxidation temperature and duration and composition[9, 23]. The lower compressive stress cannot stabilise the t-ZrO_2 after water vapor oxidation, which results in the high fraction of phase transition of m-ZrO_2. This in turn results in higher phase content ratio of m-ZrO_2/t-ZrO_2 after water vapor oxidation than that after air oxidation. It has been generally recognized that the t-ZrO_2 phase can also be stabilized by mechanisms of grain size refinement. The presence of some t-ZrO_2 phase in the outer coating layer closer to the free surface can also be explained by the presence of fine grains, which promote the stabilisation of t-ZrO_2 [16].

4.2 Porosity and Cracking in the oxide layer

As mentioned above, the ZrO_2 layer grown during water vapor oxidation is full of nanoscale porosity and cracks, whereas the oxide that grows during air oxidation shows existence of limited nanoscale cracking, as shown in the FIB and TEM images. It is highly unlikely that these pores and cracks were generated during preparation of samples as these samples for SEM or TEM were all prepared by focused ion beam milling. During the high-temperature water vapor oxidation of ZrN, the hydrogen and nitrogen gases are formed. It can be postulated that the formation of porosities could be related to the gas entrapment which could not diffuse out through the oxide layer and became entrapped. Terrani, et al., have shown that during the oxidation of SiC in water vapor environment at high temperature the pores in the SiO_2 layer are caused by the bubbles containing gaseous reaction by-products (CO and H_2)[24].

However, cracks were observed in the oxide layer whether after water vapor oxidation or air oxidation, as shown in Fig.6 and 10. The cracks are lateral and parallel to the ZrN/ZrO_2 interface and there are almost no vertical cracks detected. Garner, et al., have studied the oxidation behavior of Zr alloy after an autoclave test at 350°C, and also observed the lateral cracks across the ZrO_2 scale as well [15]. In this study, the cracks may have been generated by stress. The compressive stresses in the ZrO_2 oxide layer after water vapor and air oxidation (200MPa and 1.2GPa, respectively) will act parallel to the ZrN-ZrO_2 interface (crack direction). Thus, it is not possible for the compressive stress to generate the lateral cracks. Similarly, the tensile stress during cooling process can not contribute to the lateral cracks. Qi has studied the oxidation of ZrN and found the vertical cracks in the ZrO_2 oxide scale. This can be attributed, in this case, to the higher tensile stresses (0.8 to 1.4 GPa) or mechanical polishing during the preparation of samples[22]. In this study, it can be predicted that the lateral cracks could be generated by vertical tensile stretching. During the oxidation and cooling processes, there is continuous phase transition from t-ZrO_2 to m-ZrO_2[9, 23]. Qi studied the oxidation process of ZrN by in-situ GIXRD, which showed that the simultaneous formation of new t-ZrO_2 and the transformation from preformed t-ZrO_2 to m-ZrO_2 occurs simultaneously [9]. Yang also studied the oxidation process of Zr alloy by in-situ Raman spectroscopy, which indicated that the t-ZrO_2 phase remained constant while the m-ZrO_2 phase content increases continuously with the increase of oxidation time[23]. Furthermore, the transformation from the tetragonal ZrO_2 to monoclinic ZrO_2 would lead to an the increase of volume of 6.77% and the generation of shear strain, as shown schematically in Fig.13 [15]. The shear strain can result in out-of-plane tensile strains on surrounding materials. The Fig. 14 shows the schematic formation of lateral cracks after tetragonal-to-monoclinic transformation. When the t phase transforms to m phase, the shear stress (vertical direction) will be applied in the nearby grains and stretch the grains. If the nearby grains do not undergo phase transition， as can be indicated by t-EBSD results, and the tensile stress reaches a critical point, lateral cracks could be formed in the oxide layer at the nearby grains (red oscillating lines), as shown in Fig. 14. For a proportion of the t-ZrO_2 that underwent the phase transition, asymmetrical cracks have been formed. Furthermore, in a direction paralleling to the ZrN/ZrO_2 interface, tensile stresses are also applied during the phase transition from t-ZrO_2 to m-ZrO_2. However, the growth stress (compressive stress) can neutralize the tensile stress that develops from phase transition. Thus, the vertical cracks are not observed. The ratio of phase transition from t-ZrO_2 to m-ZrO_2 after water vapor oxidation is higher than that after air oxidation, which results in the more cracks appearing across ZrO_2 layer after water vapor oxidation. It was reported that the phase stability of t-ZrO_2 was improved by the addition of Y and that this could result in a reduction of micro-crack propagation across ZrO_2 scale during the oxidation of ZrYN coatings[25, 26]. Furthermore, the pores formed in the oxide layer contribute to the relaxation of compressive stress, which promotes the phase transition from t-ZrO_2 to m-ZrO_2. Thus, there are more cracks across ZrO_2 scale after water vapor oxidation.

4.3 Oxidation mechanism

In a high-temperature water vapor environment, water molecules are more easily dissociated compared to the O_2 molecules in air at the same temperature and the reactivity of OH^- radicals in the water vapor with the ZrN surface is much stronger than that of the oxygen molecules in the air[27]. Thus, at the initial oxidation stage, the oxidation rate of ZrN in the water vapor is several orders of magnitude higher than that in the air.

As oxidation time increases, the oxide layer becomes thicker. The oxide scale can serve as a barrier layer to restrict the inward transportation of oxidizing species. Therefore, the oxidation rate of ZrN will drop with the development of the oxide layer. Thus, the parabolic rate behavior is observed for the oxidation of ZrN in the high-temperature air and water vapor environments. However, the oxidation rate of ZrN in the water vapor is approximately 100 times higher than that of ZrN in the air, as shown in Fig. 3. The morphology and thickness of oxide scale are, therefore, key factors affecting the oxidation rate of ZrN in both water vapor and air environment. The ZrO_2 scale that has grown in water vapor after 1 hour exposure at 600°C has significantly more cracks and pores present than that grown in air at the same temperature and exposure time. These cracks and pores are believed to explain the enhanced the recession rate of ZrN in the water vapor environment. Fig.15 is a depiction of various oxide layer microstructures after ZrN oxidation in the air and water vapor[24]. In this figure, J_1 denotes the flux of oxidizing species to the ZrN/ZrO_2 interface by diffusing through the ZrO_2 layer. The J_2 denotes the transportation of oxidizing species to the ZrN/ZrO_2 interface by transporting oxidizing species through cracks and pores. During air oxidation, cracks and flaws in the ZrO_2 oxide layer are rather limited, therefore oxidation of ZrN in air is slower and is controlled by diffusion of oxidizing species. However, after oxidation in the water vapor environment, the ZrO_2 layer has a larger number of cracks and pores. Under these conditions, the transportation of oxidizing species across the ZrO_2 scale cannot be explained by simplified diffusion mechanism. Thus, the network of cracks and pores must contribute to the transportation of oxidizing species to the ZrN/ZrO_2 reaction interface in the high-temperature water vapor environment.

5. Conclusions

The oxidation behaviors and mechanisms of ZrN coatings at the 600°C water vapor and 600°C air environments have been studied. The bilayer-structure of ZrO_2 with t-ZrO_2 near the ZrN-ZrO_2 interface and m-ZrO_2 closer to the outer oxide surface were formed after water vapor or air oxidation. After water vapor oxidation, there is a higher proportion of m-ZrO_2 in the oxide layer is formed during the water vapor oxidation than after air oxidation, coupled with higher compressive stresses present in the ZrO_2 from oxidation in air. It is believed that t-ZrO_2 was formed due to oxidation initially and then m-ZrO_2 was formed due to phase transformation from t-ZrO_2.The lateral cracks across the ZrO_2 scale after water vapor or air oxidation are caused by the phase transition from t-ZrO_2 to m-ZrO_2 rather than the compressive stress or the thermal mismatch. The parabolic rate constant of ZrN at 600 ℃ oxidizing in water vapor is approximately 100 times faster than that in the air mainly due to that the variation of noted differences in oxide microstructures, more porosity and cracking of the ZrO_2 formed in the water vapor environment. The ZrN coating fabricated by reactive magnetron sputtering could provide good protection for Zr alloy at high temperature in air and it could protect the zirconium cladding from oxidation in the case of LOCA to a certain extent. It is suggested that stabilising the t-ZrO_2 phase to slow or avoid cracking in the oxide layer could lead to formation a dense oxide scale on ZrN and therefore increase the oxidation resistance of ZrN coating, which could provide the better protection for zirconium cladding from oxidation in case of LOCA.

Acknowledgments

The authors would like to thank Dr. John Warren and Mr. Gary Harrison for the kind help on the X-ray diffraction experiments.

References

[1] D.J. Park, H.G. Kim, J.Y. Park, Y.I. Jung, J.H. Park, Y.H. Koo, A study of the oxidation of FeCrAl alloy in pressurized water and high-temperature steam environment, Corrosion Science, 94 (2015) 459-465.

[2] M. Moalem, D.R. Olander, Oxidation of Zircaloy by steam, Journal of Nuclear Materials, 182 (1991) 170-194.

[3] K.A. Terrani, C.M. Parish, D. Shin, B.A. Pint, Protection of zirconium by alumina- and chromia-forming iron alloys under high-temperature steam exposure, Journal of Nuclear Materials, 438 (2013) 64-71.

[4] F. Khatkhatay, L. Jiao, J. Jian, W. Zhang, Z. Jiao, J. Gan, H. Zhang, X. Zhang, H. Wang, Superior corrosion resistance properties of TiN-based coatings on Zircaloy tubes in supercritical water, Journal of Nuclear Materials, 451 (2014) 346-351.

[5] M. Chhowalla, H.E. Unalan, Thin films of hard cubic Zr3N4 stabilized by stress, Nature materials, 4 (2005) 317-322.

[6] E. Budke, J. Krempel-Hesse, H. Maidhof, H. Schüssler, Decorative hard coatings with improved corrosion resistance, Surface and Coatings Technology, 112 (1999) 108-113.

[7] C.-S. Chen, C.-P. Liu, C.Y.A. Tsao, H.-G. Yang, Study of mechanical properties of PVD ZrN films, deposited under positive and negative substrate bias conditions, Scripta Materialia, 51 (2004) 715-719.

[8] R.W. Harrison, W.E. Lee, N. Jacobson, Mechanism and Kinetics of Oxidation of ZrN Ceramics, Journal of the American Ceramic Society, 98 (2015) 2205-2213.

[9] Z.B. Qi, Z.T. Wu, H.F. Liang, D.F. Zhang, J.H. Wang, Z.C. Wang, In situ and ex situ studies of microstructure evolution during high-temperature oxidation of ZrN hard coating, Scripta Materialia, 97 (2015) 9-12.

[10] P. Panjan, B. Navinšek, A. Cvelbar, A. Zalar, I. Milošev, Oxidation of TiN, ZrN, TiZrN, CrN, TiCrN and TiN/CrN multilayer hard coatings reactively sputtered at low temperature, Thin Solid Films, 281 (1996) 298-301.

[11] K.P. Kyung Tae Kim The high-temperature oxidation kinetics of Zr-alloy claddings in air and steam, Transactions of the Korean Nuclear Society Autumn Meeting, (2013) 24-25.

[12] D.J. Park, Y.I. Jung, H.G. Kim, J.Y. Park, Y.H. Koo, Oxidation behavior of silicon carbide at 1200°C in both air and water–vapor-rich environments, Corrosion Science, 88 (2014) 416-422.

[13] K.W. PJ Kelly, H Li, J Verran and RD Arnell, The influence of silver content on the tribological and antimicrobial properties of ZrN/Ag nanocomposite coatings., Journal of Nanoscience and Nanotechnology, 11 (2011).

[14] H.L. PJ Kelly, PS Benson, KA Whitehead, J Verran, RD Arnell and I Iordanova , 205 (2010) 1606-1610, Comparison of Tribological and Anti-Microbial Properties of CrN/Ag, ZrN/Ag, TiN/Ag, and TiN/Cu Nanocomposite Coatings, Surf. Coat. Technol., 205 (2010) 1606-1610

[15] A. Garner, A. Gholinia, P. Frankel, M. Gass, I. MacLaren, M. Preuss, The microstructure and microtexture of zirconium oxide films studied by transmission electron backscatter diffraction and automated crystal orientation mapping with transmission electron microscopy, Acta Materialia, 80 (2014) 159-171.

[16] A.T.F. M.E. Fitzpatrick, P. Holdway,, J.S.a.L.S. F.A. Kandil, Determination_of_Residual_Stresses_by_X-ray_Diffraction, Measurement Good Practice Guide, 52 (2005).

[17] Y. Chen, X. Zhao, M. Bai, A. Chandio, R. Wu, P. Xiao, Effect of platinum addition on oxidation behavior of γ/γ' nickel aluminide, Acta Materialia, 86 (2015) 319-330.

[18] E. Polatidis, P. Frankel, J. Wei, M. Klaus, R.J. Comstock, A. Ambard, S. Lyon, R.A. Cottis, M. Preuss, Residual stresses and tetragonal phase fraction characterisation of corrosion tested Zircaloy-4 using energy dispersive synchrotron X-ray diffraction, Journal of Nuclear Materials, 432 (2013) 102-112.

[19] Z.B. Qi, B. Liu, Z.T. Wu, F.P. Zhu, Z.C. Wang, C.H. Wu, A comparative study of the oxidation behavior of Cr2N and CrN coatings, Thin Solid Films, 544 (2013) 515-520.

[20] Z.T. Wu, Z.B. Qi, W.F. Jiang, Z.C. Wang, B. Liu, Influence of niobium addition on microstructure, mechanical properties and oxidation resistance of ZrN coatings, Thin Solid Films, 570 (2014) 256-261.

[21] N. Ravikumar, S. Prinz, Y. Cai, A. Zimmermann, F. Aldinger, F. Berger, K. Muller, Crystallization and creep behavior of Si–B–C–N ceramics, Acta Materialia, 53 (2005) 4567-4578.

[22] A.M. Limarga, D.S. Wilkinson, G.C. Weatherly, Modeling of oxidation-induced growth stresses, Scripta Materialia, 50 (2004) 1475-1479.

[23] F. Yang, X. Zhao, P. Xiao, In Situ Measurement of Stresses and Phase Compositions of the Zirconia Scale During Oxidation of Zirconium by Raman Spectroscopy, Oxidation of Metals, 81 (2013) 331-343.

[24] B.A.P. Kurt A. Terrani, Chad M. Parish, Chinthaka M. Silva, Lance L. Snead,* and, Y. Katoh, Silicon Carbide Oxidation in Steam up to 2 MPa, The American Ceramic Society, 97 (2014).

[25] S. Shukla, S. Seal, Mechanisms of room temperature metastable tetragonal phase stabilisation in zirconia, International Materials Reviews, 50 (2013) 45-64.

[26] Q.G. Zhou, X.D. Bai, X.Y. Xue, Y.H. Ling, X.W. Chen, J. Xu, D.R. Wang, The influence of Y ion implantation on the oxidation behavior of ZrN coating, Vacuum, 76 (2004) 517-521.

[27] J. Musil, G. Remnev, V. Legostaev, V. Uglov, A. Lebedynskiy, A. Lauk, J. Procházka, S. Haviar, E. Smolyanskiy, Flexible hard Al-Si-N films for high temperature operation, Surface and Coatings Technology, 307 (2016) 1112-1118.

Figure captions

Fig.1 Geometry of stress measurement by Bruker Discover XRD

Fig.2, (a) cross-sectional SEM images of as-deposited ZrN coating, (b) ex situ GIXRD patterns of the as-deposited ZrN coating.

Fig.3 Change in oxide thickness of oxidized ZrN at 600ºC air and water vapor environment as a function of time

Fig.4 Cross-sectional images of ZrN coatings by milled FIB after water vapor oxidation: (a) coating exposed for 0.5hour at 600°C in the water vapor environment; (b) for 1 hour at 600°C in water vapor (c) for 1 minute at 1200°C in the water vapor environment.

Fig.5 Ex situ GIXRD patterns of the ZrN coating after oxidation at 600°C water vapor environment for 1 hour

Fig.6 Cross-sectional TEM image of the oxidized ZrN coating after water vapor oxidation at 600°C for 1 hour

Fig.7 t-EBSD phase map of cross-sectional ZrO_2 layer (monoclinic ZrO_2 is shown in blue colour, tetragonal ZrO_2 is shown in green colour, red box area for TKD analysis)

Fig.8 Cross-sectional SEM images of the oxidized ZrN coating after oxidation in the air at: (a) 600°C for 1 hour; (b) 600°C for 4 hours; (c) 600°C for 8 hours

Fig.9 Ex situ GIXRD patterns of the ZrN coating after oxidation in the air at 600°C for 8 hours

Fig.10 Cross-sectional image of the oxidized ZrN coating after air oxidation at 600°C for 1 hour: (a) TEM image; (b) EDS line of oxygen and nitrogen counts in the line in the Fig. 10a.

Fig.11 t-EBSD phase map of cross-sectional ZrO_2 layer formed on the top of ZrN coating after 1 hour at 600°C in air (monoclinic ZrO_2 is shown in blue colour, tetragonal ZrO_2 is shown in green colour, red box area for T-EBSD analysis).

Fig.12 A typical plot of (-1 1 1) of m-ZrO_2 d-spacing against $\sin^2\psi$ in measuring the oxide scales; (a) after 1 hour in water vapor at 600°C, (b) after 8 hour in air at 600°C

Fig. 13 Schematic of tetragonal-to-monoclinic transformation in ZrO_2

Fig. 14 Schematic formation of lateral cracks after tetragonal-to-monoclinic transformation in ZrO_2 (tetragonal is black colour, monoclinic is green colour, red oscillating line is crack)

Fig.15 Depiction of various oxide layer microstructures after ZrN oxidation in air and water vapor

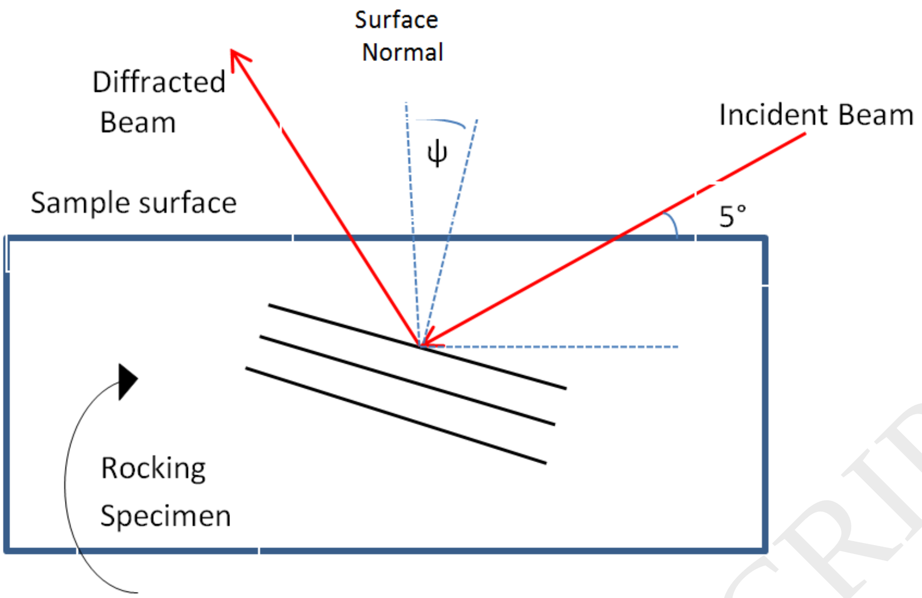
Surface
Normal
Diffracted
Beam
ψ
Incident Beam
Sample surface
5°
Rocking
Specimen

Fig.1

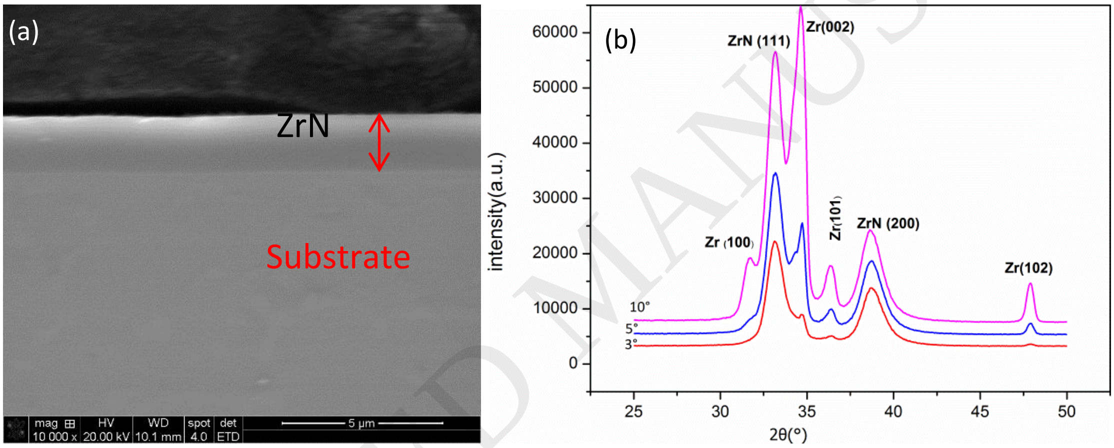
(a)
ZrN
Substrate
mag 10 000 x
HV 20.00 kV
WD 10.1 mm
spot 4.0
det ETD
5 µm
(b)
ZrN (111)
Zr(002)
Zr (100)
Zr(101)
ZrN (200)
Zr(102)
10°
5°
3°
intensity(a.u.)
2θ(°)
0
10000
20000
30000
40000
50000
60000
25
30
35
40
45
50

Fig.2

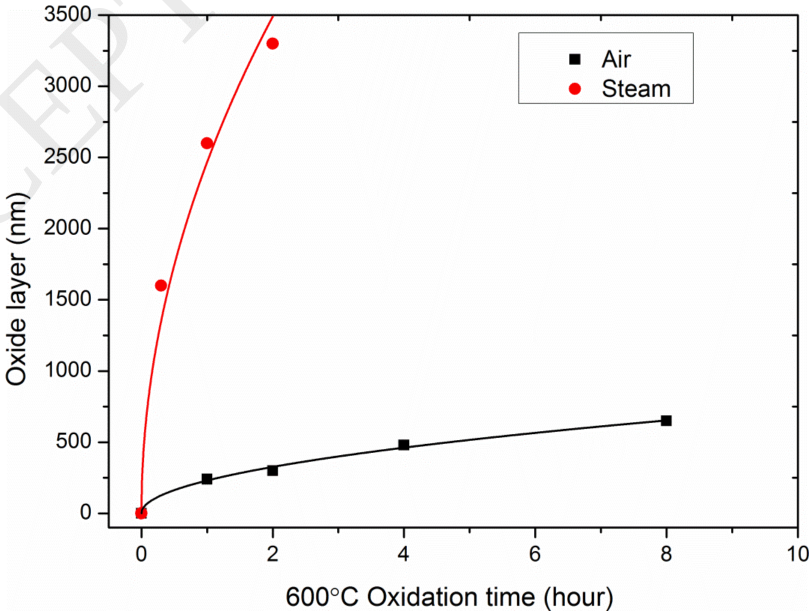
■ Air
● Steam
Oxide layer (nm)
600°C Oxidation time (hour)
0
500
1000
1500
2000
2500
3000
3500
0
2
4
6
8
10

Fig.3

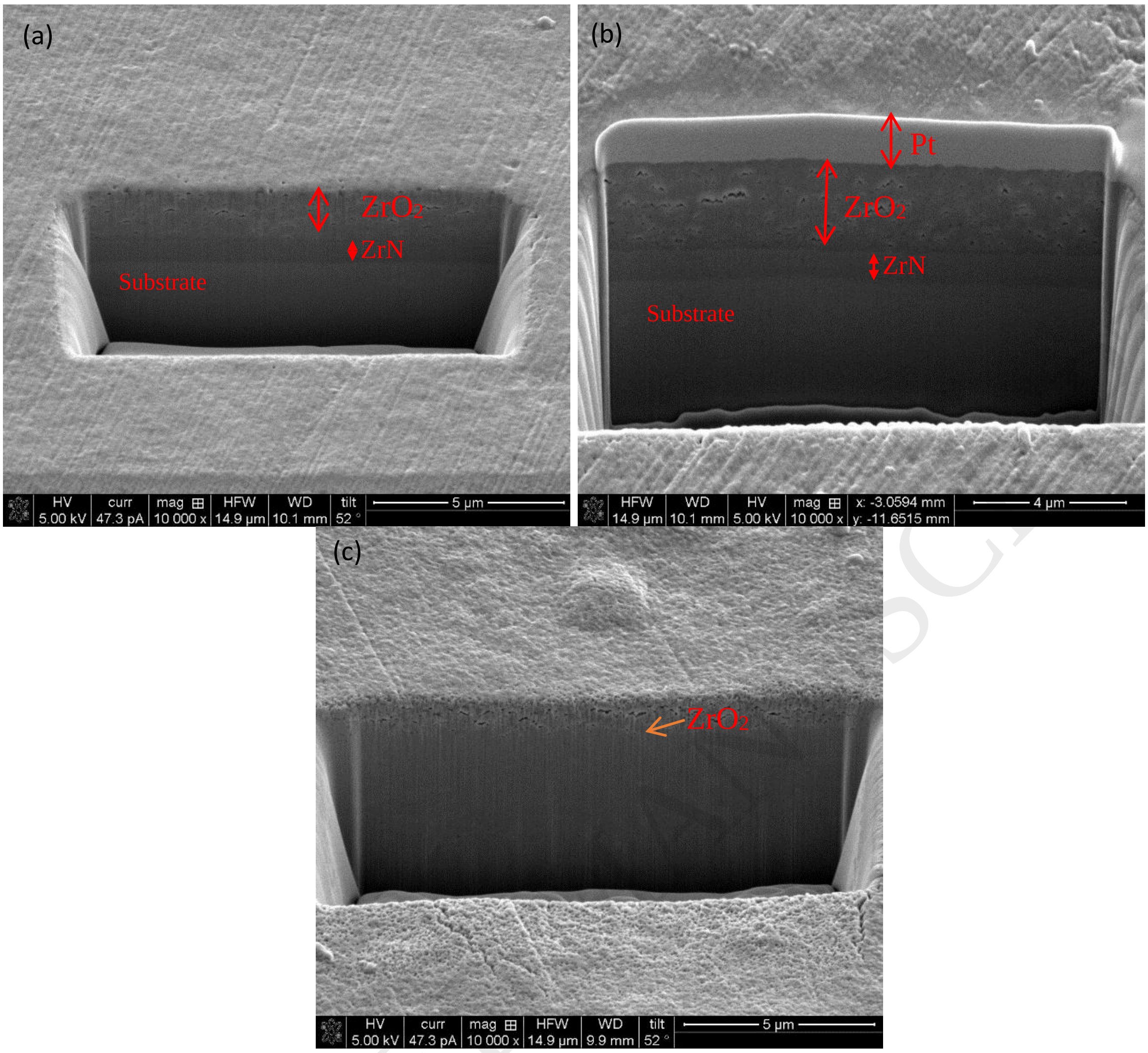
(a)
ZrO$_2$
ZrN
Substrate
HV 5.00 kV | curr 47.3 pA | mag 10 000 x | HFW 14.9 µm | WD 10.1 mm | tilt 52 ° | 5 µm
(b)
Pt
ZrO$_2$
ZrN
Substrate
HFW 14.9 µm | WD 10.1 mm | HV 5.00 kV | mag 10 000 x | x: -3.0594 mm y: -11.6515 mm | 4 µm
(c)
ZrO$_2$
HV 5.00 kV | curr 47.3 pA | mag 10 000 x | HFW 14.9 µm | WD 9.9 mm | tilt 52 ° | 5 µm

Fig.4

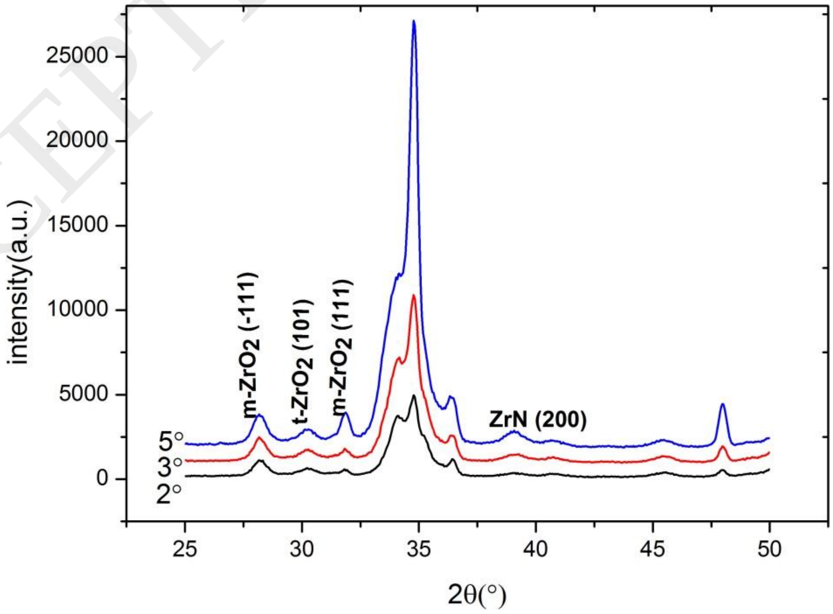
intensity(a.u.)
25000
20000
15000
10000
5000
0
m-ZrO$_2$ (-111)
t-ZrO$_2$ (101)
m-ZrO$_2$ (111)
ZrN (200)
5°
3°
2°
25
30
35
40
45
50
2θ(°)

Fig.5

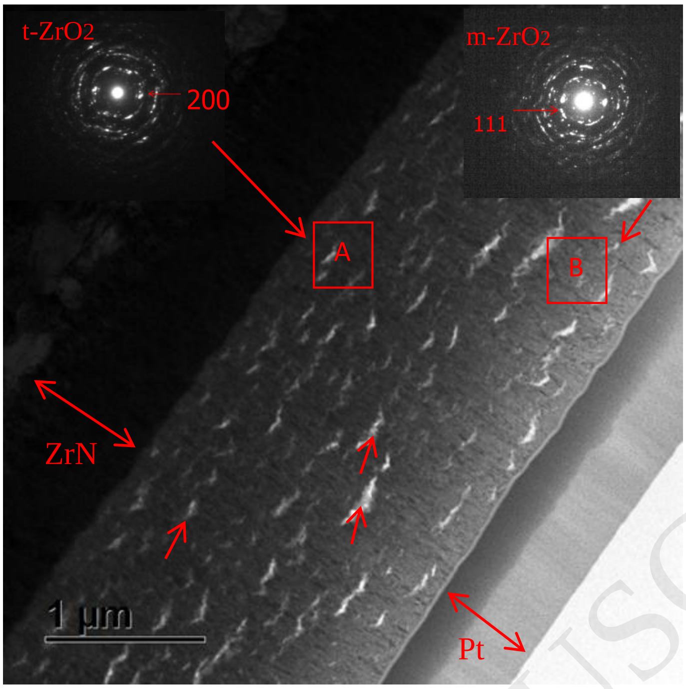

Fig.6

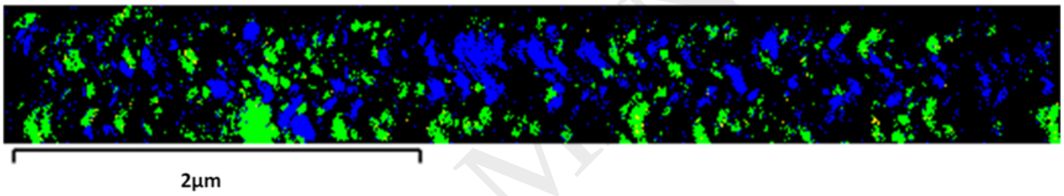

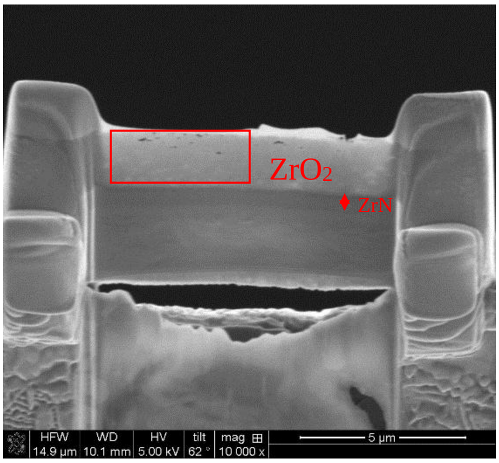
ZrO2
ZrN
HFW 14.9 µm
WD 10.1 mm
HV 5.00 kV
tilt 62 °
mag 10 000 x
5 µm

Fig.7

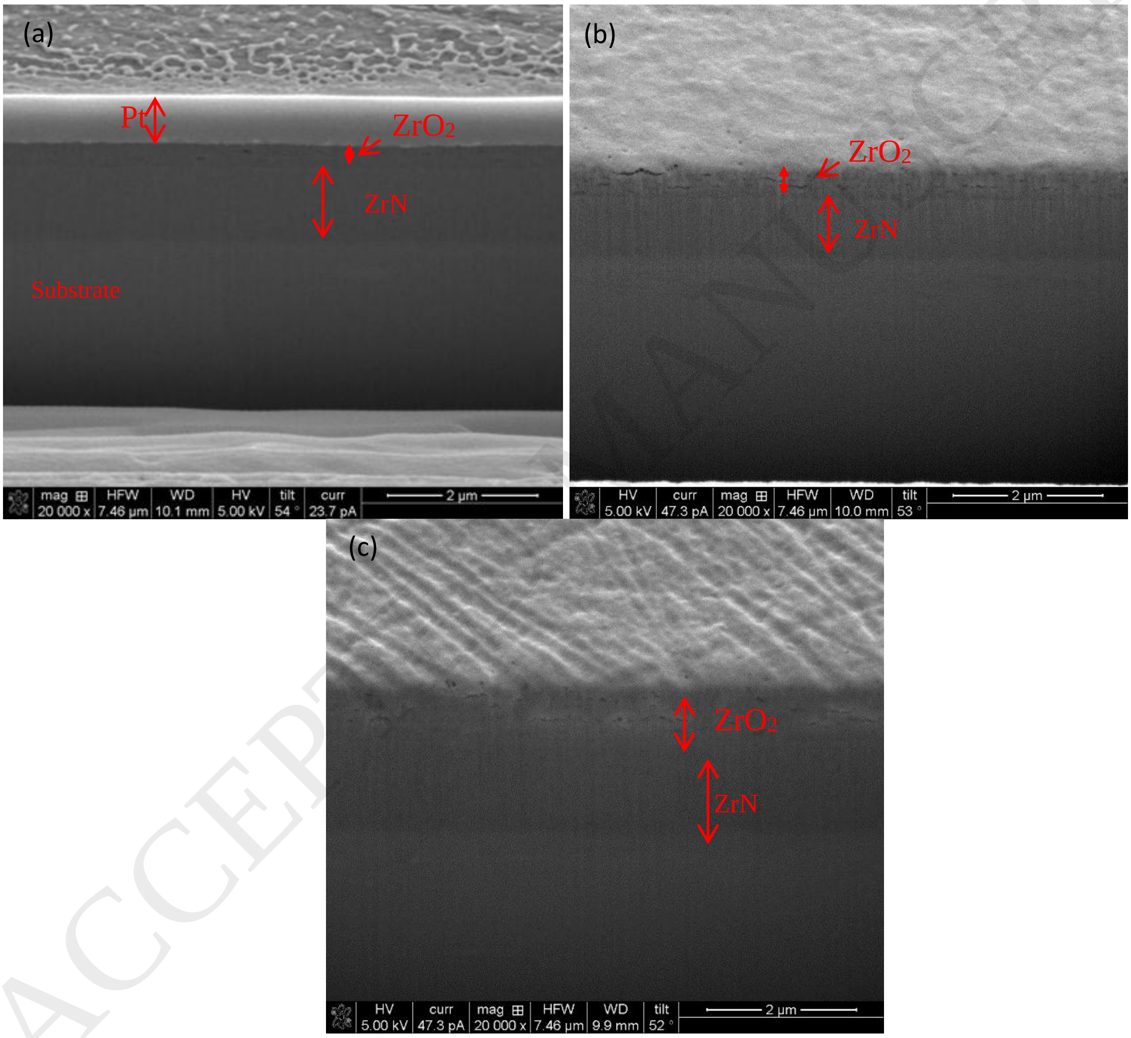
(a)
Pt
ZrO2
ZrN
Substrate
mag 20 000 x
HFW 7.46 µm
WD 10.1 mm
HV 5.00 kV
tilt 54 °
curr 23.7 pA
2 µm
(b)
ZrO2
ZrN
HV 5.00 kV
curr 47.3 pA
mag 20 000 x
HFW 7.46 µm
WD 10.0 mm
tilt 53 °
2 µm
(c)
ZrO2
ZrN
HV 5.00 kV
curr 47.3 pA
mag 20 000 x
HFW 7.46 µm
WD 9.9 mm
tilt 52 °
2 µm

Fig.8

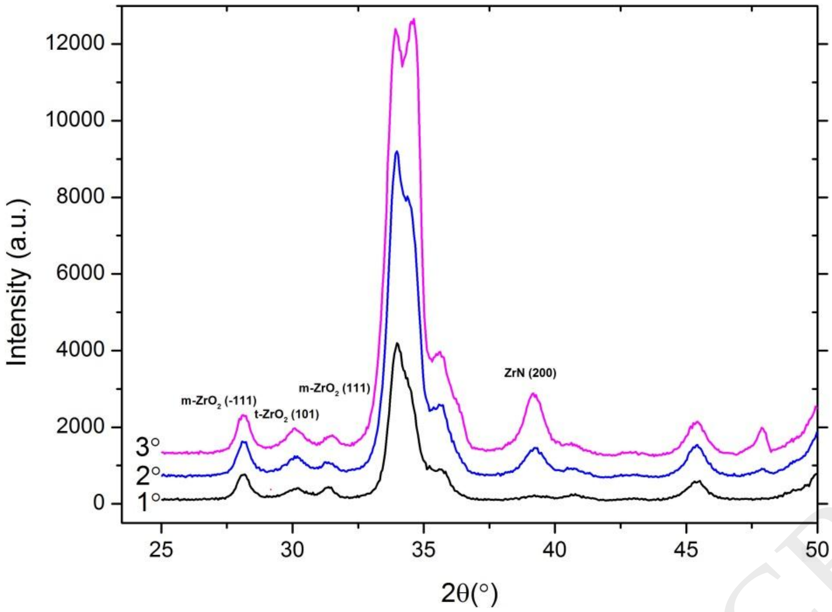
12000
10000
8000
6000
4000
2000
0
Intensity (a.u.)
25
30
35
40
45
50
2θ(°)
m-ZrO2 (-111)
t-ZrO2 (101)
m-ZrO2 (111)
ZrN (200)
3°
2°
1°

Fig.9

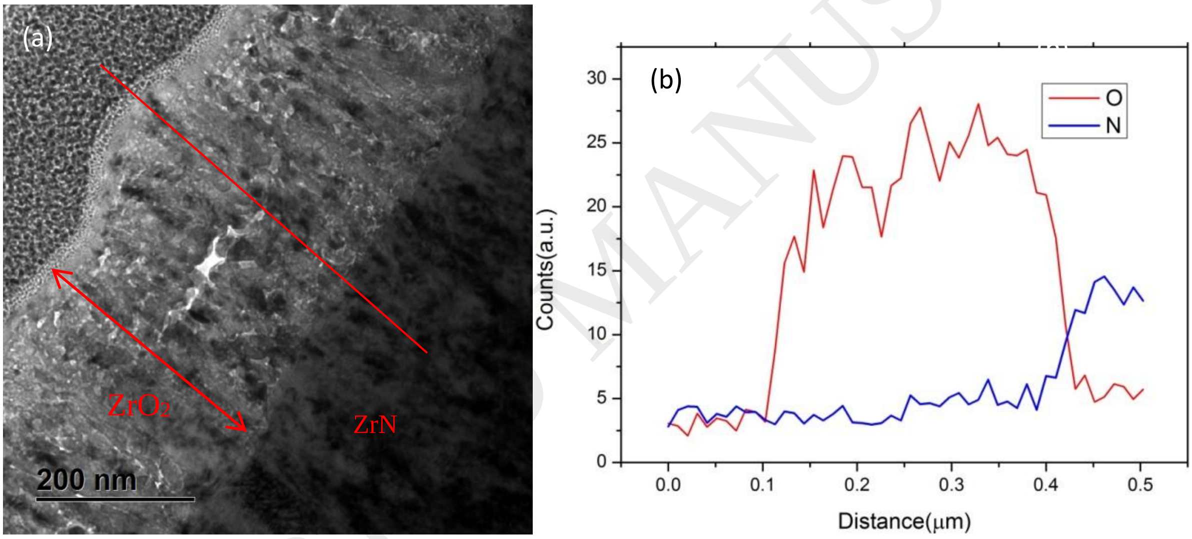
(a)
ZrO2
ZrN
200 nm
(b)
O
N
30
25
20
15
10
5
0
Counts(a.u.)
0.0
0.1
0.2
0.3
0.4
0.5
Distance(μm)

Fig.10

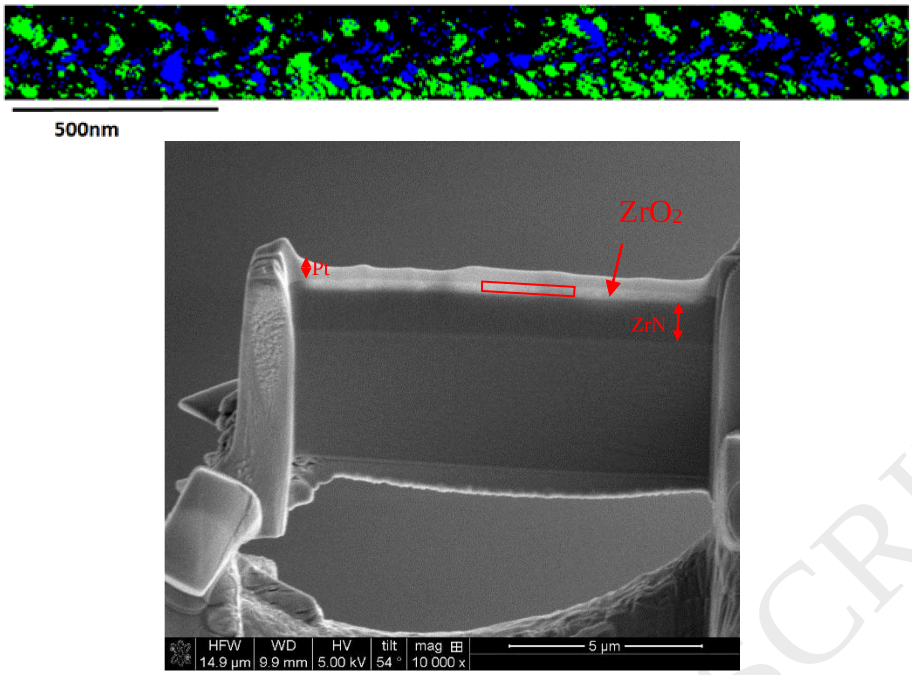
500nm
ZrO2
Pt
ZrN
HFW 14.9 µm
WD 9.9 mm
HV 5.00 kV
tilt 54 °
mag ⊞ 10 000 x
5 µm

Fig.11

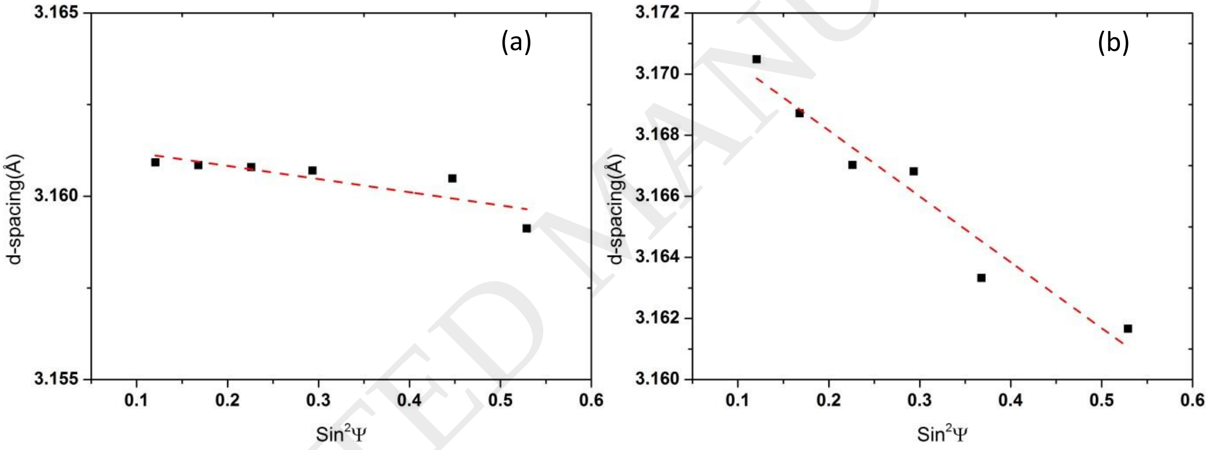
(a)
(b)
d-spacing(Å)
Sin²Ψ
3.155
3.160
3.165
3.160
3.162
3.164
3.166
3.168
3.170
3.172
0.1
0.2
0.3
0.4
0.5
0.6

Fig.12

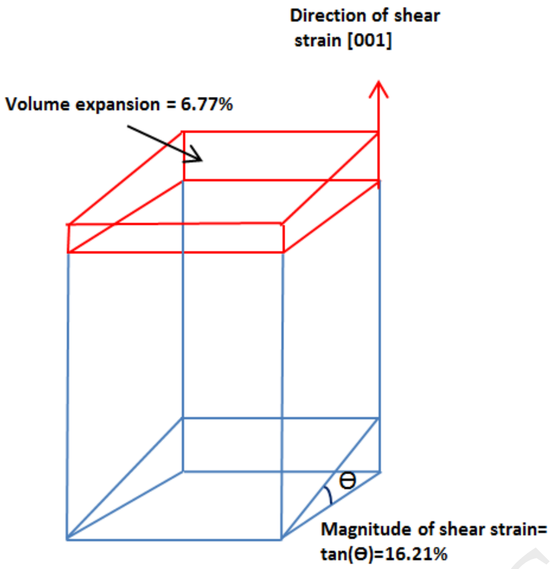

Fig. 13

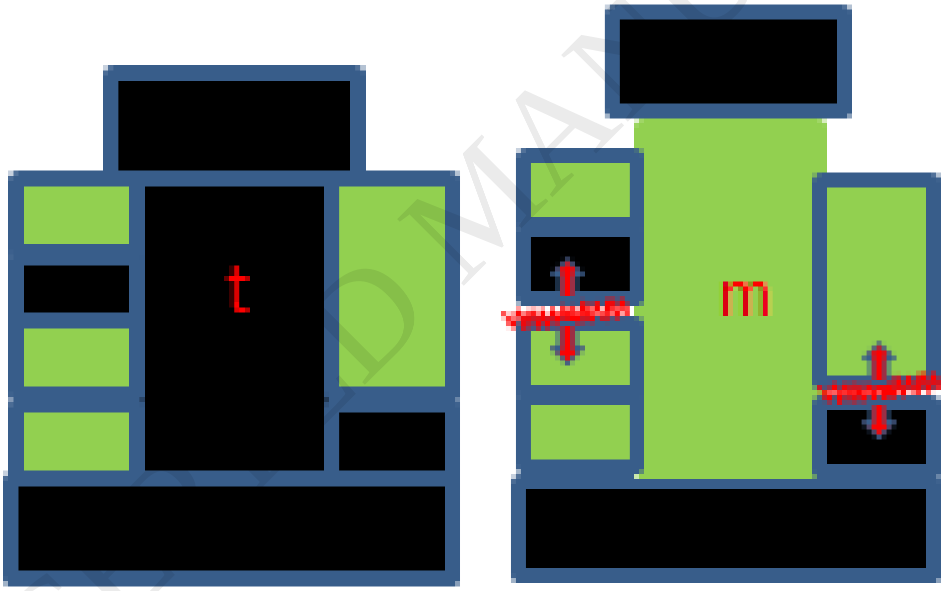

Fig. 14

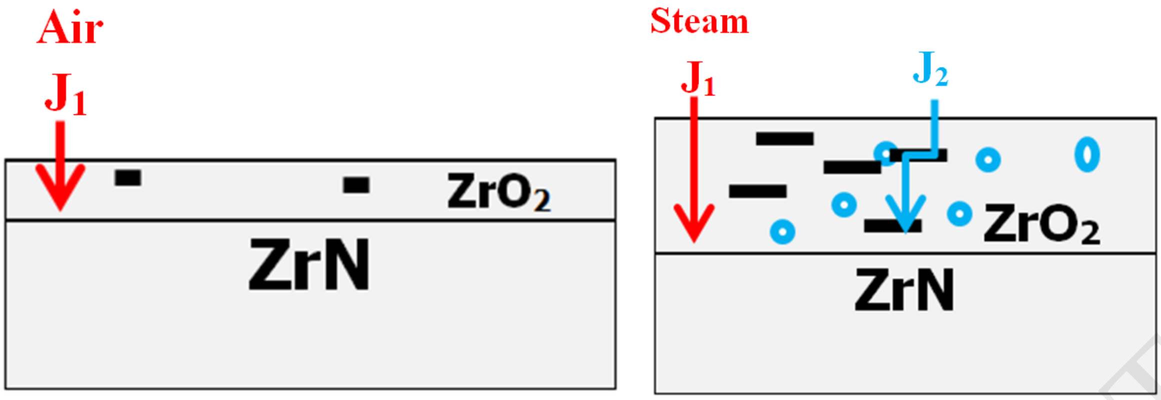

Fig.15